Radar Sounding of the Medusae Fossae Formation Mars: Equatorial Ice or Dry, Low-Density Deposits?

Thomas R. Watters, *et al.*

Science **318**, 1125 (2007);
DOI: 10.1126/science.1148112

Science (print ISSN 0036-8075; online ISSN 1095-9203) is published weekly, except the last week in December, by the American Association for the Advancement of Science, 1200 New York Avenue NW, Washington, DC 20005.

the point that our autocatalyst could be used as an enzyme-free constant-temperature alternative to PCR for detecting known sequences.

For many applications in biotechnology, nucleic acid devices must remain functional in the presence of naturally occurring macromolecules. We therefore tested the autocatalyst system in the presence of an excess of mouse liver total RNA with rabbit reticulocyte lysate (Fig. 4E). Reactions proceeded to apparent completion with no more than a twofold slowdown, and the presence of a 3% trigger can still be detected.

The ability to construct larger circuits will enable the wide range of chemical circuit functions needed for sophisticated applications. Our entropy-driven catalytic reaction networks are suited for scaling up to larger circuits. The modular molecular design makes synthesis of more complex components and networks with arbitrary topology straightforward. To demonstrate this, we constructed an entropy-driven catalytic analog AND gate in which both of two catalysts are required to release output (SOM text S12 and fig. S11). For scaling up to large circuits, independent catalyst systems must have negligible crosstalk. The success of quantitative models that assume no crosstalk, as presented above, is encouraging; further evidence comes from a test of two independent catalyst systems operating in the same solution (fig. S12). Finally, catalytic systems have the potential to avoid the slowdown that plagued previous attempts to construct large nucleic acid circuits (*17*).

Future nucleic acid control circuits must be interfaced to molecular sensors and actuators. This may be achieved directly when the inputs and outputs are themselves nucleic acids, such as for the detection, analysis, and response to complex nucleic acid samples (*9*, *30*) or for the control of nucleic acid nanomachines (*2*, *31*). Nucleic acid circuits can also respond to and control more general chemical events: In principle, the release of an oligonucleotide could regulate covalent chemistry by controlling (deoxy)ribozyme activity (*9*) or reactant proximity (*32*). Additionally, signals carried by small organics and other non–nucleic acid molecules can be read by nucleic acid systems with the use of aptamer domains (*33*, *34*) and other binding interactions that can regulate toehold accessibility (*35*, *36*). Thus, nucleic acids could provide a general-purpose system for the synthesis of embedded control circuitry within aqueous chemical systems.

References and Notes

1. R. F. Gesteland, T. R. Cech, J. F. Atkins, Eds. *The RNA World: The Nature of Modern RNA Suggests a Prebiotic RNA World* (Cold Spring Harbor Laboratory Press, Cold Spring Harbor, NY, ed. 3, 2006).
2. N. C. Seeman, *Trends Biochem. Sci.* **30**, 119 (2005).
3. J. Bath, A. J. Turberfield, *Nat. Nanotechnol.* **2**, 275 (2007).
4. G. F. Joyce, *Annu. Rev. Biochem.* **73**, 791 (2004).
5. A. J. Turberfield *et al.*, *Phys. Rev. Lett.* **90**, 118102 (2003).
6. J. S. Bois *et al.*, *Nucleic Acids Res.* **33**, 4090 (2005).
7. G. Seelig, B. Yurke, E. Winfree, *J. Am. Chem. Soc.* **128**, 12211 (2006).
8. S. J. Green, D. Lubrich, A. J. Turberfield, *Biophys. J.* **91**, 2966 (2006).
9. M. N. Stojanovic, T. E. Mitchell, D. Stefanovic, *J. Am. Chem. Soc.* **124**, 3555 (2002).
10. J. Macdonald *et al.*, *Nano Lett.* **6**, 2598 (2006).
11. H. Lederman, J. Macdonald, D. Stefanovic, M. N. Stojanovic, *Biochemistry* **45**, 1194 (2006).
12. M. Hagiya, S. Yaegashi, K. Takahashi, in *Nanotechnology: Science and Computation*, J. Chen, N. Jonoska, G. Rozenberg, Eds. (Springer, New York, 2006), pp. 293–308.
13. M. Levy, A. D. Ellington, *Proc. Natl. Acad. Sci. U.S.A.* **100**, 6416 (2003).
14. R. M. Dirks, N. A. Pierce, *Proc. Natl. Acad. Sci. U.S.A.* **101**, 15275 (2004).
15. M. N. Stojanovic *et al.*, *J. Am. Chem. Soc.* **127**, 6914 (2005).
16. R. Penchovsky, R. R. Breaker, *Nat. Biotechnol.* **23**, 1424 (2005).
17. G. Seelig, D. Soloveichik, D. Y. Zhang, E. Winfree, *Science* **314**, 1585 (2006).
18. In the system presented in Fig. 1, there is some sequence redundancy in the domain sequences chosen (for example, 2b and 5 are identical). This is because all four systems presented in this paper were designed together, with the goal of minimizing the number of differences between systems. In the design of a catalytic reaction in isolation, there are no sequence constraints; we demonstrate a system with completely independent catalyst and output in SOM text S10; it has very similar kinetics to that of the reaction shown in Fig. 1.
19. M. Zuker, *Nucleic Acids Res.* **31**, 3406 (2003).
20. J. Sager, D. Stefanovic, in *DNA Computing: 11th International Workshop on DNA Computing*, A. Carbone, N. A. Pierce, Eds. (Springer, Berlin, 2006), pp. 275–290.
21. K. U. Mir, in *DNA-Based Computers II: DIMACS Workshop*, L. F. Landweber, E. B. Baum, Eds. (American Mathematical Society, Providence, RI, 1999), pp. 243–246.
22. B. Yurke, A. P. Mills, *Genet. Program. Evolvable Mach.* **4**, 111 (2003).
23. I. G. Panyutin, P. Hsieh, *J. Mol. Biol.* **230**, 413 (1993).
24. Materials and methods (SOM text S2) are available as supporting material on *Science* Online.
25. S. A. Marras, F. R. Kramer, S. Tyagi, *Nucleic Acids Res.* **30**, e122 (2002).
26. C. Green, C. Tibbetts, *Nucleic Acids Res.* **9**, 1905 (1981).
27. R. Higuchi, C. Fockler, G. Dollinger, R. Watson, *Nat. Biotechnol.* **11**, 1026 (1993).
28. N. Paul, G. F. Joyce, *Curr. Opin. Chem. Biol.* **8**, 634 (2004).
29. P. Yin, H. M. T. Choi, C. R. Calvert, N. Pierce, *Nature*, in press.
30. Y. Benenson, B. Gil, U. Ben-Dor, R. Adar, E. Shapiro, *Nature* **429**, 423 (2004).
31. R. Pei *et al.*, *J. Am. Chem. Soc.* **128**, 12693 (2006).
32. X. Li, D. R. Liu, *Angew. Chem. Int. Ed.* **43**, 4848 (2004).
33. A. D. Ellington, J. Szostak, *Nature* **346**, 818 (1990).
34. J. Tang, R. R. Breaker, *Chem. Biol.* **4**, 453 (1997).
35. S. Müller, D. Strohbach, J. Wolf, *Proc. IEEE Nanobiotechnol.* **153**, 31 (2006).
36. F. J. Isaacs, D. J. Dwyer, J. J. Collins, *Nat. Biotechnol.* **24**, 545 (2006).

37. We thank X. R. Bao, G. Seelig, D. Soloveichik, P. Rothemund, and L. Adleman for insightful discussions. There is a patent pending on this work. D.Y.Z. and A.J.T. were supported by UK research councils (Engineering and Physical Sciences Research Council, Biotechnology and Biological Sciences Research Council, Medical Research Council, and the Ministry of Defence) though the Bionanotechnology Interdisciplinary Research Collaboration. D.Y.Z. and E.W. were supported by a Caltech Grubstake Grant and NSF grants 0506468, 0622254, and 0533064. D.Y.Z. is supported by the Fannie and John Hertz Foundation.

Supporting Online Material

www.sciencemag.org/cgi/content/full/318/5853/1121/DC1
SOM Text S1 to S12
Figs. S1 to S12
Tables S1 to S4
References

30 July 2007; accepted 8 October 2007
10.1126/science.1148532

Radar Sounding of the Medusae Fossae Formation Mars: Equatorial Ice or Dry, Low-Density Deposits?

Thomas R. Watters,[1]* Bruce Campbell,[1] Lynn Carter,[1] Carl J. Leuschen,[2] Jeffrey J. Plaut,[3] Giovanni Picardi,[4] Roberto Orosei,[4] Ali Safaeinili,[3] Stephen M. Clifford,[5] William M. Farrell,[6] Anton B. Ivanov,[3] Roger J. Phillips,[7] Ellen R. Stofan[8]

The equatorial Medusae Fossae Formation (MFF) is enigmatic and perhaps among the youngest geologic deposits on Mars. They are thought to be composed of volcanic ash, eolian sediments, or an ice-rich material analogous to polar layered deposits. The Mars Advanced Radar for Subsurface and Ionospheric Sounding (MARSIS) instrument aboard the Mars Express Spacecraft has detected nadir echoes offset in time-delay from the surface return in orbits over MFF material. These echoes are interpreted to be from the subsurface interface between the MFF material and the underlying terrain. The delay time between the MFF surface and subsurface echoes is consistent with massive deposits emplaced on generally planar lowlands materials with a real dielectric constant of ~2.9 ± 0.4. The real dielectric constant and the estimated dielectric losses are consistent with a substantial component of water ice. However, an anomalously low-density, ice-poor material cannot be ruled out. If ice-rich, the MFF must have a higher percentage of dust and sand than polar layered deposits. The volume of water in an ice-rich MFF deposit would be comparable to that of the south polar layered deposits.

Units of the Medusae Fossae Formation (MFF) occur discontinuously at equatorial latitudes along the boundary of the hemispheric dichotomy from Amazonis to Elysium Planitiae (~130°E to 240°E) (*1*, *2*). The MFF may be among the youngest surficial deposits on Mars, unconformably overlying ancient Noachian heavily cratered highlands and young Amazonian lowlands (*1*–*8*). However, pedestal craters on the outer edge of the MFF

deposits have been cited as evidence of an older age (*9*). The local topographic relief of the MFF units varies greatly, reaching a maximum of more than 3.5 km (*5*–*7*). The morphology of the MFF units is complex and variable. Over large horizontal scales (tens of kilometers), the undulating hills of the MFF are relatively smooth (Fig. 1). At smaller scales, many of the MFF units are marked by systems of parallel ridges and grooves interpreted as yardangs (*10*–*14*) (Fig. 2). Remnant yardangs and outliers some distance from the thicker units suggest that MFF deposits once covered a larger area of the northern lowlands (*3*, *6*) (Fig. 2A). Layering is observed in the MFF deposits that varies in scale from coarse, indurated layers that cap weaker, more friable material to thin, pervasive layering (*3*, *4*, *6*, *15*–*17*).

A variety of origins have been proposed for the MFF deposits. These include ignimbrite or volcanic ash deposits from now-buried vents (*1*, *2*, *6*, *11*), eolian deposits from materials weathered early in martian history (*1*, *18*), and deposits analogous to polar layered and circumpolar deposits formed either as a consequence of polar wandering (*9*) or during periods of high obliquity (*7*) [see supporting online material (SOM) text]. Units of the MFF are associated with the "Stealth" region on Mars (SOM text), so named because no echo is detected in 3.5- and 12.6-cm Earth-based radar data (*19*–*21*).

We report here on observations of the MFF deposits by the MARSIS radar sounder (*22*) (SOM text). Subsurface echoes are detected that correspond to the basal interface between the MFF material and the underlying plains material. We also characterize the thickness and electrical properties of the MFF deposits as a guide to their bulk porosity and/or ice fraction.

MARSIS data obtained between March 2006 and April 2007 cover all the units of the MFF (Fig. 1). Radargrams, or time-delay renderings of the sounding data along the spacecraft ground track, show subsurface echoes, offset in time-delay from the surface return, where the tracks cross the MFF (Fig. 3). The subsurface echoes generally parallel the surface return except near the margins where, in some cases, the subsurface and surface echoes converge (Fig. 3). The observed time-delay in the radargrams is consistent with the expected depth to the interface between the MFF deposits and the underlying terrain.

The westernmost MFF deposits form low-relief, undulating hills (Fig. 1) and overlie relatively young (Late Amazonian-aged) lowlands volcanic plains associated with Cerberus Fossae (*2*, *8*) (Fig. 2A). The inferred elevation of the subsurface interface corresponds closely with the floor of a valley separating two hills where MFF material has been almost completely stripped away, nearly exposing the Cerberus plains (Fig. 2B and Fig. 3A). The MFF material that forms Lucus Planum is deposited on older (Hesperian-aged), lowlands knobby terrain (*2*, *8*) (Fig. 1). The interface beneath the eastern flank of this unit is flat and largely continuous (Fig. 3B). The MFF material exposed in the pronounced valley of Medusae Fossae itself extends from the northern lowlands into the ancient heavily cratered (Noachian-aged) southern highlands, locally burying the dichotomy boundary and the cratered highlands (*2*, *8*) (Fig. 1). A generally flat, continuous subsurface interface that extends for several hundred kilometers is separated in time-delay from a shallower, discontinuous interface associated with a layer internal to the MFF deposits (Fig. 3C). The subsurface echo from the eastern flank of Eumenides Dorsum is more spread out in time-delay but appears to delineate the north-downward slope of the buried dichotomy boundary (Fig. 3D). MFF material overlying Amazonian-period volcanic plains (*1*, *8*) forms the prominent ridges of Amazonis Mensa and Gordii Dorsum (Fig. 1). There are two parallel subsurface echoes from the valley between the ridges (Fig. 3E) that correspond to the base of the MFF material and an internal dielectric horizon. The discontinuous subsurface echoes associated with the northern tip of Gordii Dorsum correlate in time-delay with the basal echo from the valley floor (Fig. 3E, far right in radargram). The easternmost MFF deposits overlie the dichotomy boundary and Amazonian volcanic plains of Olympus Mons and the Tharsis Montes (*1*) and narrow northwestward into a ridge (Fig. 1). A discontinuous subsurface reflection from beneath the western part of the ridge suggests a flat basal interface (Fig. 3F).

Previous analyses suggested that some MFF units are draped over preexisting topographic rises in the lowlands (*13*, *23*). The subsurface interfaces revealed by MARSIS suggest that MFF materials are deposited on generally planar materials in the northern lowlands and the downward slope of the dichotomy boundary (Fig. 3).

[1]Center for Earth and Planetary Studies, National Air and Space Museum, Smithsonian Institution, Washington, DC 20560, USA. [2]Center for Remote Sensing of Ice Sheets, University of Kansas, Lawrence, KS 66045, USA. [3]Jet Propulsion Laboratory, California Institute of Technology, Pasadena, CA 91109, USA. [4]Infocom Department, "La Sapienza" University of Rome, 00184 Rome, Italy. [5]Lunar and Planetary Institute, 3600 Bay Area Boulevard, Houston, TX 77058, USA. [6]NASA/Goddard Space Flight Center, Greenbelt, MD 20771, USA. [7]Department of Earth and Planetary Sciences, Washington University, St. Louis, MO 63130, USA. [8]Proxemy Research, Laytonsville, MD 20882, USA.

*To whom correspondence should be addressed. E-mail: watterst@si.edu

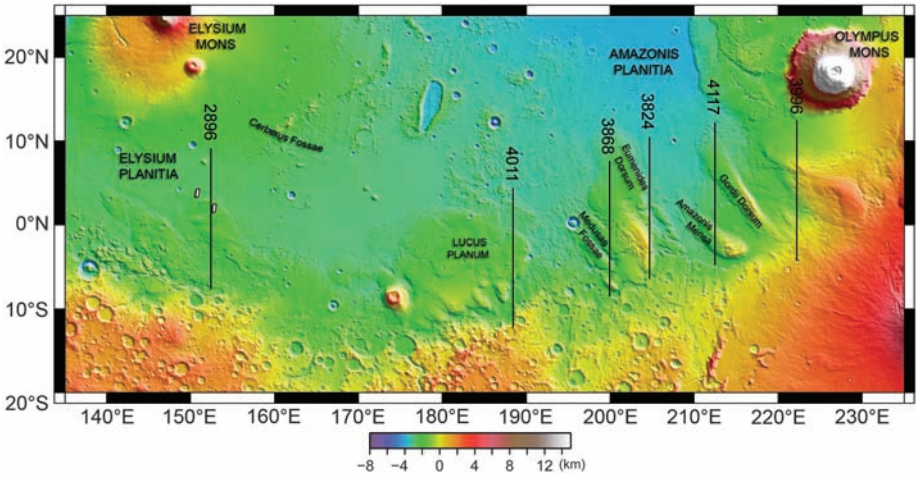

Fig. 1. The Medusae Fossae Formation in Elysium and Amazonis Planitiae along the dichotomy boundary. The locations of MARSIS orbit tracks 2896, 4011, 3868, 3824, 4117, and 3996 are indicated by back lines (from left to right, respectively) overlaid on Mars Orbiter Laser Altimeter (MOLA) color-coded shaded relief. The locations of Thermal Emission Imaging System (THEMIS) images shown in Fig. 2 are indicated by the small white rectangles.

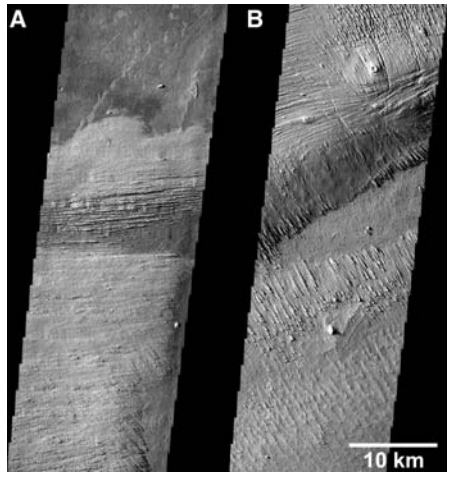

Fig. 2. High-resolution THEMIS images of the MFF material in Elysium Planitia. (**A**) THEMIS visible image (frame #V05275021) shows an outlier of MFF material that is being stripped, partially exposing the underlying lowlands plains. (**B**) THEMIS visible image (frame #V13163010) shows numerous yardangs and a valley stripped of MFF material. The locations of images (A) and (B) are to the left and right, respectively, of orbit track 2896 shown in Fig. 1.

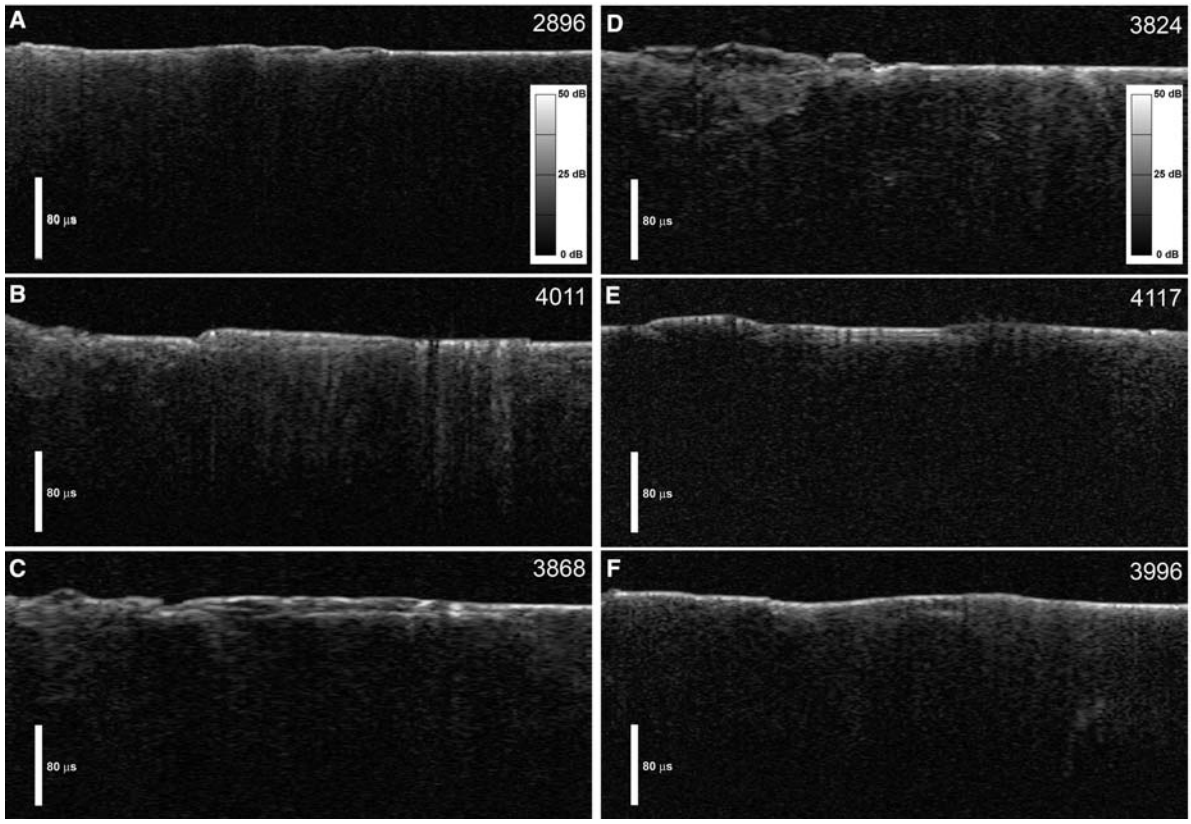

Fig. 3. Radargrams showing MARSIS data for orbit 2896 (**A**), 4011 (**B**), 3868 (**C**), 3824 (**D**), 4117 (**E**), and 3996 (**F**). Echoes are plotted in time-delay versus position along the orbit. The subsurface echoes are offset in time-delay from the surface echo and are interpreted to be nadir reflections from the interface between the MFF deposits and the lowland plains material. The peak surface return is corrected to agree with the MOLA topography along the orbit track. The radargrams are resampled to a uniform along-track length of ~1000 km. All the orbits are ascending except for orbit 2896.

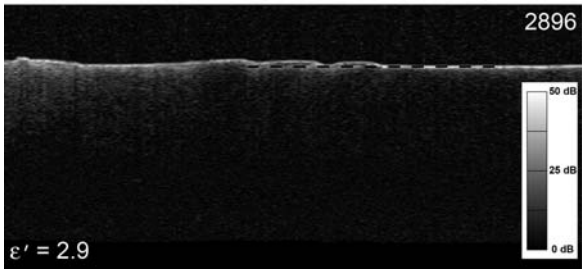

Fig. 4. Radargram showing MARSIS data for orbit 2896 converted to depth using a dielectric constant $\varepsilon' = 2.9$ for the MFF material. The dashed black line shows the projection of the lowland plains beneath the MFF deposits. There is good agreement between the basal reflector and the projection of the exposed surrounding plains (compare with Fig. 3A).

MARSIS data support estimates of the total volume of MFF material calculated using apparent base-level elevations in the lowlands. These estimates range from 1.4×10^6 km^3 (*4*) to 1.9×10^6 km^3 (*6*).

MARSIS observations provide an opportunity to evaluate the electrical properties of the MFF where the material is deposited on lowlands plains that are exposed nearby (Fig. 2A). The observed time delays in the MFF deposits correspond to a bulk real dielectric constant ε' of ~2.9 ± 0.4 (SOM text and fig. S1), based on the projection of the surrounding plains beneath the material (Fig. 4). A variation in ε' of 2.5 to 3.3 does not result in a large range in the radar-predicted thickness because h is a function of $\sqrt{\varepsilon'}$. The dielectric properties of a material are related to its density and composition. The real part of the dielectric constant is modulated strongly by density. The imaginary component of the dielectric constant ε'' and the loss tangent, $\tan\delta = \varepsilon''/\varepsilon'$, are strongly influenced by target composition. Radar losses due to attenuation in the deposits were estimated using the method outlined in Porcello *et al*. (*24*). At 4 MHz center frequency (Band 3), we obtain losses of ~0.0048 ± 0.0024 dB/m (SOM text, fig. S2). For ε' of 2.9 and a center frequency of 4 MHz, these losses correspond to a range in loss tangent of ~0.002 to 0.006 (SOM text).

MARSIS studies of the PLD (*22*, *25*) suggest a ε' value of about 3, consistent with pure water ice, based on the agreement between the inferred depth of the basal interface and the projection of the surrounding surface. The loss tangent of the PLD is estimated to range from <0.001 to 0.005 (*22*, *25*). Our analysis suggests a similar real dielectric constant (2.5 to 3.3) and a comparably low range of loss tangent (0.002 to 0.006) for the MFF materials. The loss tangents derived for the MFF deposits are below the range measured for terrestrial volcanic materials (*26*) but comparable to some low-titanium lunar materials (*27*). Thus, our first-order estimates of the dielectric losses span a range that includes some dry, unconsolidated geologic materials and mixtures of pure water ice and sediment. The real dielectric constant of the MFF and PLD deposits is also low relative to the behavior of compacted rock-derived materials, which are well fit by a function of the form $\varepsilon' = 1.96^d$, where d is the density in g/cm^3 (*26*). A maximum ε' of 3.3 corresponds to an average density of about ~1.8 g/cm^3, which is low for the expected self-compaction of 0.5 to 2.5 km of a dry geologic material.

There are two plausible interpretations of these observations. The first is that the MFF material is poorly consolidated and comprised of non-ice material with low dielectric loss. If the MFF material is an ice-poor ash or eolian deposit, it must have an unusually high porosity and low bulk density at depths up to 2.5 km to account for the estimated values of ε'. MFF deposits with a depth-averaged bulk density >1.9 g/cm^3 will have an ε' value outside the measured range.

The second possibility is that the MFF material is ice-rich, with a non-ice component of higher real dielectric constant and loss tangent (ice present as a minor component within a matrix of $\varepsilon' = 6$ does not match the observed properties). The extensive fields of yardangs in the MFF deposits, landforms that occur in variably indurated to poorly consolidated material that is easily eroded by wind (*1*–*3*, *5*, *6*, *15*), suggests that sublimation must have removed volatiles from the putative ice-rich deposits to

leave meters of dust and sand. The accumulation of meters of sediments suggests that the non-ice component of an ice-rich MFF deposit may be larger than the maximum 10% estimated for the south polar layered deposits (SPLD) (*25*). This, in turn, suggests a higher modeled real dielectric constant than that of pure ice.

Although the real dielectric constant and dielectric losses may be consistent with an ice-rich material, the existing data do not exclude the possibility that the MFF deposits are an anomalously low density, ice-poor material. In either case, these deposits appear to have unique characteristics from other martian deposits studied to date by radar sounding. An ice-rich MFF raises the intriguing possibility of a large volume of water ice in the equatorial zone of Mars beneath a veneer of dust and sand. MARSIS observations suggest that the total volume of ice in the SPLD is ~1.6×10^6 km^3 (*25*). If the MFF deposits are ice-rich, estimates of their total volume suggest a volume of water comparable to that in the SPLD.

References and Notes

1. D. H. Scott, K. L. Tanaka, *U.S. Geol. Surv. Misc. Invest. Ser.* Map, I-1802-A (1986).
2. R. Greeley, J. E. Guest, *U.S. Geol. Surv. Misc. Invest. Ser.* Map, I-1802-B (1987).
3. B. A. Bradley, S. E. H. Sakimoto, H. Frey, J. R. Zimbelman, *J. Geophys. Res.* **107**, 5058 (2002).
4. P. D. Lanagan, A. S. McEwen, L. P. Keszthelyi, T. Thordarson, *Geophys. Res. Lett.* **28**, 2365 (2001).
5. J. Zimbelman *et al., Lunar Planet. Sci.* **30**, 1652 (abstr.) (1999).
6. B. M. Hynek, R. J. Phillips, R. E. Arvidson, *J. Geophys. Res.* **108**, 5111 (2003).
7. J. W. Head and M. Kreslavsky, *Lunar Planet. Sci.* **35**, 1635 (abstr.) (2004).
8. K. L. Tanaka, J. A. Skinner, T. M. Hare, *U.S. Geol. Surv. Misc. Invest. Ser.*, Map I-2888 (2005).
9. P. H. Schultz, A. B. Lutz, *Icarus* **73**, 91 (1988).
10. A. W. Ward, *J. Geophys. Res.* **84**, 814 (1979).
11. F. El-Baz, C. S. Breed, M. J. Grolier, J. F. McCauley, *J. Geophys. Res.* **84**, 8205 (1979).
12. D. H. Scott, K. L. Tanaka, *J. Geophys. Res.* **87**, 1179 (1982).
13. S. E. H. Sakimoto, H. V. Frey, J. B. Garvin, J. H. Roark, *J. Geophys. Res.* **104**, 24141 (1999).
14. G. L. Wells, J. R. Zimbelman, in *Arid Zone Geomorphology: Process, Form and Change in Drylands*, D. S. G. Thomas, Ed. (Wiley, New York, 1997), pp. 659–690.
15. M. C. Malin *et al.*, *Science* **279**, 1681 (1998).
16. M. C. Malin, K. S. Edgett, *J. Geophys. Res.* **106**, 23429 (2001).
17. Evidence of coarse and thin layering is found in HiRISE images of both eastern and western MFF units (see HiRISE frame # TRA_000828_1805, TRA_000865_1905, PSP_002279_1735) (*28*).
18. M. H. Carr, *Water on Mars* (Oxford University Press, New York, 1996).
19. D. O. Muhleman, B. J. Butler, A. W. Grossman, M. A. Slade, *Science* **253**, 1508 (1991).
20. J. K. Harmon, R. E. Arvidson, E. A. Guinness, B. A. Campbell, M. A. Slade, *J. Geophys. Res.* **104**, 14065 (1999).
21. K. S. Edgett, B. J. Butler, J. R. Zimbelman, V. E. Hamilton, *J. Geophys. Res.* **102**, 21545 (1997).
22. G. Picardi *et al.*, *Science* **310**, 1925 (2005).
23. J. M. Dohm *et al.*, *J. Geophys. Res.* **106**, 12301 (2001).
24. L. J. Porcello *et al.*, *Proc. IEEE* **62**, 769 (1974).
25. J. J. Plaut *et al.*, *Science* **316**, 92 (2007).
26. F. T. Ulaby *et al.*, *Microwave Dielectric Spectrum of Rocks* (Univ. of Michigan, Ann Arbor, 1988).
27. W. D. Carrier, G. R. Olhoeft, W. Mendell, in *Lunar Sourcebook* (Cambridge Univ. Press, New York, 1991), pp. 475–594.
28. A. S. McEwen *et al., Lunar Planet Sci.* 38, 2031 (abstr.) (2007).

29. We are grateful to the other members of the MARSIS Science team and to the instrument operation staff. MARSIS is managed by the Agenzia Spaziale Italiana (ASI) and NASA. The Mars Express mission is managed and operated by the European Space Agency. The research activities of the MARSIS PI and Italian investigators are supported by grants under the Mars Express/ASI program. Work of the U.S. investigators is supported by grants under the Mars Express/NASA project.

Supporting Online Material

www.sciencemag.org/cgi/content/full/1148112/DC1
SOM Text
Figs. S1 and S2
References

20 July 2007; accepted 4 October 2007
Published online 1 November 2007;
10.1126/science.1148112
Include this information when citing this paper.

Three-Dimensional Splay Fault Geometry and Implications for Tsunami Generation

G. F. Moore,[1,2]* N. L. Bangs,[3] A. Taira,[1] S. Kuramoto,[1] E. Pangborn,[3] H. J. Tobin[4]

Megasplay faults, very long thrust faults that rise from the subduction plate boundary megathrust and intersect the sea floor at the landward edge of the accretionary prism, are thought to play a role in tsunami genesis. We imaged a megasplay thrust system along the Nankai Trough in three dimensions, which allowed us to map the splay fault geometry and its lateral continuity. The megasplay is continuous from the main plate interface fault upwards to the sea floor, where it cuts older thrust slices of the frontal accretionary prism. The thrust geometry and evidence of large-scale slumping of surficial sediments show that the fault is active and that the activity has evolved toward the landward direction with time, contrary to the usual seaward progression of accretionary thrusts. The megasplay fault has progressively steepened, substantially increasing the potential for vertical uplift of the sea floor with slip. We conclude that slip on the megasplay fault most likely contributed to generating devastating historic tsunamis, such as the 1944 moment magnitude 8.1 Tonankai event, and it is this geometry that makes this margin and others like it particularly prone to tsunami genesis.

Most of Earth's largest and most destructive earthquakes and tsunamis occur along the global belt of subduction zones (*1*–*4*). Great (moment magnitude > 8.0) earthquakes are generated when large areas of the subduction megathrust rupture, a process that often generates large tsunamis such as those produced by the 2004 Sumatra and 2006 Java earthquakes (*5*, *6*). The size and destructive power of tsunamis that often accompany great subduction earthquakes is determined largely by the amount and area of vertical uplift of the sea bed, and these factors are especially sensitive to the geometry of the slipping fault as the earthquake rupture approaches the sea floor (*7*–*9*). Very long thrust faults that rise from the plate boundary megathrust and intersect the sea floor along the lower slope of the margin—known as out-of-sequence or megasplay faults and recently identified as first-order features in the Nankai Trough (*10*, *11*)—are also common in other subduction zones such as Alaska (*12*, *13*), Sunda (*14*), and Colombia (*15*). These megasplay faults have been hypothesized to efficiently transfer displacement to the near surface, fostering tsunami genesis, but owing to the lack of resolution of the shallow structure of these faults, the capability of the megasplay in enhancing tsunami generation has been controversial (*16*, *17*). Moreover, an earthquake that ruptures up to (or near) the surface (i.e., one with a slip distribution skewed to the updip end) has an enhanced tsunamigenic potential (*18*).

The Nankai Trough is characterized by destructive earthquakes that occur repeatedly along the plate boundary megathrust (*19*). A large out-of-sequence thrust (OOST), first recognized as a strong seismic reflection (*10*), branches from the megathrust fault ~50 km landward of the trench south of Kii Peninsula, where it forms the trenchward boundary of Kumano Basin (Fig. 1). Swath-bathymetric and seismic reflection data show a pronounced, continuous outer ridge of topography that extends more than 120 km along the strike (Figs. 1 and 2) and is related to the splay fault slip. This fault, termed the "megasplay" (*11*), is a fundamental structural element of the margin. Substantial long-term slip is documented by sequence boundaries and progressive landward tilting of the strata in Kumano Basin (*3*).

[1]Center for Deep Earth Exploration, Japan Agency for Marine Earth Science and Technology, 3173-25 Showa-machi Kanazawa-ku, Yokohama, Japan. [2]Department of Geology and Geophysics, University of Hawaii, Honolulu, HI 96822, USA. [3]University of Texas Institute for Geophysics, J. J. Pickle Research Campus, Building 196, 10100 Burnet Road (R2200), Austin, TX 78758–4445, USA. [4]Department of Geology and Geophysics, University of Wisconsin, Madison, WI 53706, USA.

*To whom correspondence should be addressed. E-mail: gmoore@jamstec.go.jp